Article

A Comprehensive Design and Experiment of a Biplane Quadrotor Tail-Sitter UAV

Zheng Qiao [1,2,3], Dong Wang [1,2,3], Jiahui Xu [3], Xinbiao Pei [1,3], Wei Su [3], Dong Wang [4] and Yue Bai [1,2,*]

[1] Changchun Institute of Optics, Fine Mechanics and Physics, Chinese Academy of Sciences, Changchun 130033, China; qiaozheng19@mails.ucas.ac.cn (Z.Q.); wangdong21b@mails.ucas.ac.cn (D.W.); peixinbiao@ciomp.ac.cn (X.P.)

[2] University of Chinese Academy of Sciences, Beijing 100049, China

[3] Changchun Changguang Boxiang UAV Co., Ltd., Changchun 130033, China; xujiahui@bxuav-ciomp.com (J.X.); 15543196327@163.com (W.S.)

[4] China North Vehicle Research Institute, Beijing 100072, China; wangdong173@mails.ucas.ac.cn

*   Correspondence: baiy@ciomp.ac.cn

Abstract: Tail-sitter unmanned aerial vehicles (UAVs) are promising vertical takeoff and landing (VTOL) UAV suitable for multi-missions but the road to the commercialization of tail-sitter UAVs is tortuous. This paper aims to provide a systematic design methodology and present the development process for a novel biplane quadrotor tail-sitter UAV platform named TW10 to accelerate commercialization of this type of UAV. All the design choices and trade-offs in aerodynamics, structure, avionics, and the control scheme are detailed. A simulation and real flight test results are demonstrated to prove the feasibility of our design methodology. TW10 can carry a 1 kg mission load to achieve more than 2.5 h of flight time. This work serves as a meaningful reference for the promotion of tail-sitter UAVs in practical industrial applications.

Keywords: UAV; VTOL; tail-sitter; fixed wing; dynamic modeling; controller investigation; simulation; outdoor flight

1. Introduction

In recent years, unmanned aerial vehicles (UAV) have been utilized in various applications, both civil and military. One of the most popular rotary-wing UAVs is the quadrotor. Rotary-wing UAVs are widely used in the civilian consumer market for aerial photography, first-person view (FPV) entertainment [1], and other scenarios. Due to the weakness of battery capacity of small UAVs [2], the UAVs used in the industry urgently require longer flight endurance, larger payload capacity, and faster flight speed, such as wastewater detection [3], river features extraction [4], and high-voltage power transmission line autonomous inspection [5]. In industrial application, users prefer to choose VTOL UAVs out of the lack of airport. The common hybrid vertical takeoff and landing (VTOL) UAV has received extensive attention from surveillance [6], emergency transportation [7], and search and rescue [8] for accurate displacement monitoring [9] because it does not require an airport to takeoff. Due to its high convenience, small hybrid UAVs have shown explosive growth in the civilian market.

In the past, academic research on unmanned aerial vehicles (UAVs) still focused on rotor-wing UAVs and fixed-wing UAVs. Due to technological progress, the aerodynamic layout and structural forms of unmanned aerial vehicles are becoming more diverse and the exploration of drone application scenarios is becoming richer. Small UAVs account for the vast majority of the market share due to their lower price and convenience. Small UAVs refer to remotely controlled or autonomous aircraft with an empty aircraft weight of no more than 15 kg or a maximum takeoff weight of no more than 25 kg [10]. Currently, there are several common hybrid vertical takeoff and landing unmanned aerial vehicles,

including tail-sitter [11–13], tiltrotor [14,15], and tiltwing compound helicopter [15,16] concepts. Coban, S. realized simultaneous improvement of the longitudinal and lateral flight trajectory tracking performances for hybrid VTOL UAV [17]. A VTOL hybrid blended-wing-body-based UAV is proposed for intruder inspections [18]. Wang developed a small battery-powered hand-toss fixed-wing UAV with fly-wing configuration [19]. The tail-sitter UAV has received widespread attention due to its advantage of eliminating the power system tilting mechanism, thereby reducing dead weight to prolong flight endurance. In order to achieve excellent energy consumption performance, propeller pitch control devices have been installed on unmanned aerial vehicles to solve the contradiction between the vertical takeoff and landing phase and the cruise flight phase of the propeller [20]. However, for small UAVs, this design greatly increases the structural complexity and production cost. Three challenges are faced by all hybrid UAV types, which include aerodynamic tradeoffs to provide excellent performance, lightweight structure optimization to prolong endurance, and robust controller design to ensure flight stability. The tail-sitter UAV is receiving a lot of attention because of its simple mechanical structure and easy operation [12]. However, it is vulnerable to gusts during the hovering stage [21] and has difficulty building up enough airspeed to generate lift during the transition stage. The typical operation mode of a tail-sitter is divided into three modes, including VTOL mode, forward flight mode, and transition mode, as shown in Figure 1. During the transition phase, tail-sitter UAVs often fly at high angles of attack, making it difficult to establish sufficient airspeed, and face strong aerodynamic nonlinearity, which brings great difficulties for modeling and control [22].
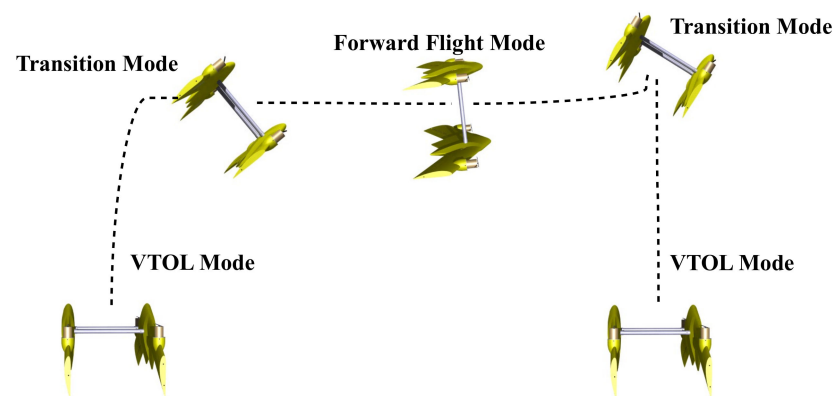

Figure 1. Tail-sitter mission profile.

Stable attitude control outweighs all other parameters of the tail-sitter UAV, a highly nonlinear plant, and is easily affected by uncertainties, such as external aerodynamics, unmodeled disturbance, and parameter perturbations. Attitude controller design often pays close attention to the VTOL mode and transition controller design. With respect to VTOL mode, most academic research results were concerned with the robustness of controller to improve the attitude accuracy against external turbulence [21,23,24]. Ahmed and Li employed the model reference adaptive control (MRAC) scheme for VTOL mode in attempting to alleviate the impact of gust and wind disturbance [21,23]. Liu designed a series of robust controllers by combining robust control and gain scheduling control to guarantee robust stability and satisfactory performance [24]. However, the robustness of an MRAC control system depends on adaptive gains, while large gains always weaken system stability [25,26]. Based on MRAC architecture, Cao proposed L1 adaptive control theory [26,27]. L1 adaptive control ensures that the error remains within a certain limit during the rapid adaptation process by introducing a low-pass filter during the flight-phase switch process [28]. Capello et al. applied L1 adaptive control to a small flying UAV attitude loop controller [29]. Multi-controller schemes which employ gain scheduling control struggle to guarantee global stability in the switching process. L1 adaptive control could eliminate the shortcomings of gain scheduling control.

Generally speaking, biplane quadrotor tail-sitter UAVs usually have quad fixed-pitch rotors and dual wings without a stagger angle because of the necessity of keeping the plane motor level [30]. Raj. N. developed a novel swiveling biplane quadrotor tail-sitter; its upper and lower wings twist around the roll axis to use the propeller pull component to generate yaw torque to enhance yaw channel control capabilities [30]. This kind of configuration improves compactness and the control margin by sacrificing the lift-to-drag ratio to a certain degree [31]. This scheme is appropriate for micro UAV but not suitable for larger aircraft. Therefore, we can conclude that biplane quad rotor tail-sitters are able to enhance the wind resistance and smoothness of the transition process in the pitch and roll channel, further reducing the likelihood of air crashes. Furthermore, if the distance between the upper and lower wings is more than 1.5 times the chord length, inter-wing interference can be ignored [31].

In this paper, we propose a tail-sitter UAV named TW10. The complete design procedure, manufacturing technique, and flight tests are detailed. This is a bold attempt of tail-sitter UAV to enter the civil market. Based on TW10′s development experience, we aim to develop a larger biplane quadrotor tail-sitter UAV suitable for various scenarios such as transporting emergency medical goods, urban logistics, aerial unmanned travelling, and carrying passengers as unmanned aircraft. The special design of TW10 aims to achieve flexible, efficient, and safe flight. Before products are introduced to the civilian market, both hardware platforms and flight control systems should undergo extensive testing to avoid accidents involving personal injury or death.

The structure of the remaining sections of this manuscript is as follows: we present a detailed introduction to design methodology of TW10 in Section 2, including aerodynamics, structure, propulsion, and avionics design. In addition, the manufacturing process of the aircraft is briefly summarized. The complete aircraft dynamic model which laid the foundation for controller design is analyzed in Section 3. The controller design for the full envelope of TW10 is carefully designed using L1 adaptive and cascaded control structures in Section 4. In Section 5, the results of UAV simulation and real flight are shown and discussed.

2. Product Design Steps and Precautions

The design methodology of this paper is shown in Figure 2, which demonstrates detailed thinking throughout our aircraft designing and manufacturing process.
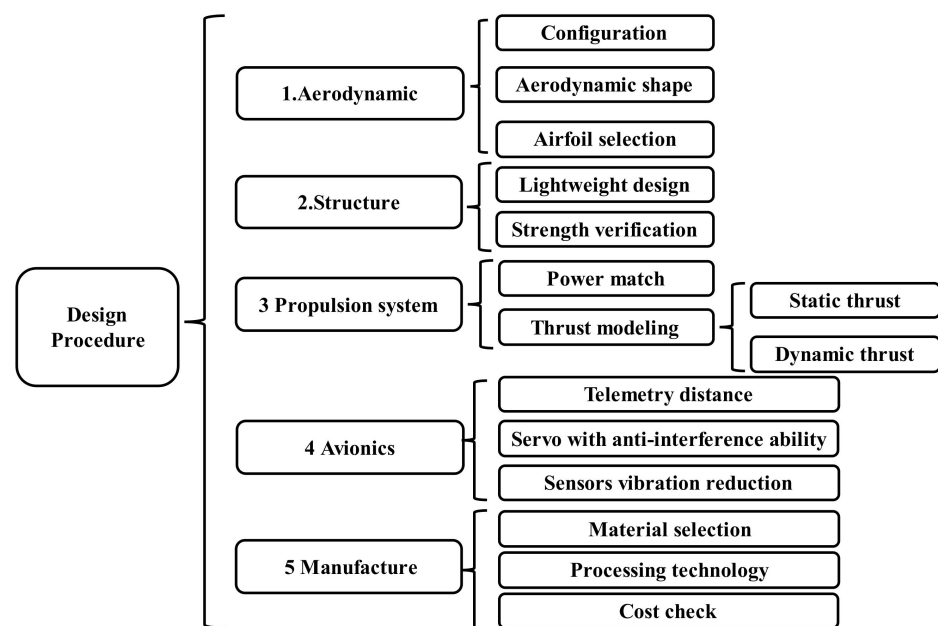

Figure 2. Design procedure.

2.1. Design Procedure

2.1.1. Applicable Requirements

Clear applicable scenarios and detailed design indicators, such as takeoff weight, flight duration, cruise airspeed, wingspan, and target load, are given. Different application scenarios lead to completely different product designs. The design procedure is a complicated process which requires elaborate market research, supply chain communication, and team technological accumulation assessment. Considering the above factors, the specifications of an aircraft for aerial survey are listed in Table 1.

Table 1. Design specifications.

Design Parameter	Value
Maximum Takeoff weight	$\geq$10 kg
Wing span	$\leq$2 m
Maximum Payload	>1 kg
Flight endurance	$\geq$120 min
Cruise speed	$\geq$13 m/s

2.1.2. Conceptual Design

At this stage, the aerodynamic shape, structure configuration, and propulsion system avionics are preliminarily designed. Aerodynamic design consists of airfoil selection, aerodynamic shape sizing, control surface design considering prop wash, and detailed computational fluid dynamics (CFD) computation. Structure design requires the consideration of portability and lightweight design for user convenience, as well as a long flight range. A propulsion system should not only provide sufficient thrust in the hover stage and transition stage, but also work with high efficiency and low power consumption during the cruise phase, which is a thorny issue for fixed-pitch propellers.

2.1.3. System Verification and Optimization

Structural strength verification and the circular optimization of structural parameterization for lightweight aircraft are conducted with the aim of increasing the flight endurance and the load capacity. Moreover, the specifications of the signal line, power line, steering engine, envelope material, and propulsion system must be determined.

2.1.4. Manufacturing and Test

A key point in manufacturing is the selection of aircraft mold material. The machining accuracy, surface roughness, manufacturing difficulty, and cost of different material molds vary. With respect to wing skin material, fiberglass-reinforced plastics, steel, aluminum, and phenolic plastics are common materials used in mold manufacturing. The phenolic plastic mold is a cheap option; however, the deformation of this mold gradually increases with the increase in the frequency of use. With the aid of a master mold, fiberglass-reinforced plastic mold is a practical way to rapidly realize mass production. However, the surface accuracy of the master mold is usually poor, which can decrease wing surface consistency. Steel and aluminum molds possess better surface roughness but they are expensive and heavy. After careful consideration, we chose a steel mold to fabricate our verification aircraft.

Extensive flight testing is critical to an aircraft's commercialization process. Numerous parameters need to be tested, including stall speed, cruise speed, flight range, flight endurance, aerodynamic coefficients verification, etc. An aircraft should be tested in a variety of environmental conditions to prove its stability and security.

2.2. Aerodynamic Design

For TW10, we adopted the blended-wing-body (BWB) technique to design the aircraft's aerodynamic shape so that both the body and wing could provide lift in the transition phase and forward flight phase. We used the torque generated by the differential thrust

of the propeller to play a role in the vertical tail so that the lightweight design was much simpler to realize. Thus, no vertical tail-flying wing design was adopted. Furthermore, considering the lateral stability, a favorable sweep angle could be added.

For tail-sitter in VTOL mode, considering vulnerability to wind, reducing the windward area to improve wind resistance is an appropriate idea despite the sacrifice of the increase in cruise speed. Moreover, the position relationship between center of the gravity and aerodynamic focus (AF) should be adjusted carefully to provide certain longitudinal stability. With respect to TW10, the center of gravity is positioned ahead of the focal point at a distance of 10% of the mean aerodynamic chord length, and a relatively small pitch trim moment is needed.

2.2.1. Fuselage and Wing Design

The first principle of BWB airfoil selection for the fuselage is to select an airfoil of a certain thickness to meet the installation requirements of batteries, avionics, and other necessary payloads. On the premise of satisfying the first principle, a high-lift and low-drag airfoil is considered to provide more lift. High lift always leads to a large nose-down moment, which is vital to fly wing configuration without a real elevator to stabilize the pitch channel. With respect to wing airfoil selection, a high-lift and low-drag airfoil which is relatively easy to trim in the longitudinal channel should be chosen. Based on the above considerations, a B-29-root airfoil was selected for the fuselage with a 21.98% maximum thickness and an NACA 4415 airfoil was selected for the wing. The aerodynamic coefficients of the B-29-root airfoil and NACA 4415 airfoil are illustrated in Figures 3 and 4 from 0–90° angle of attack (AOA).
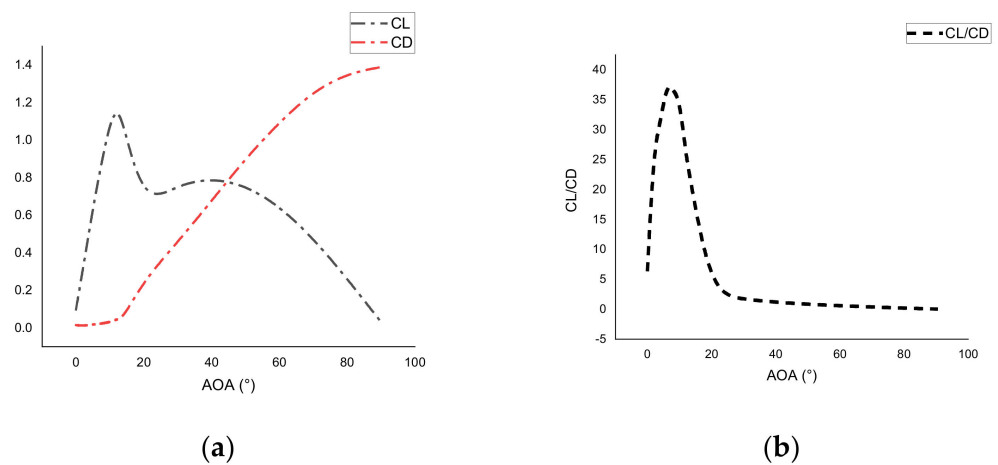

(a) **(b)**

Figure 3. B—29-root airfoil aerodynamic performance: (**a**) lift and drag coefficient; (**b**) lift—to—drag ratio.
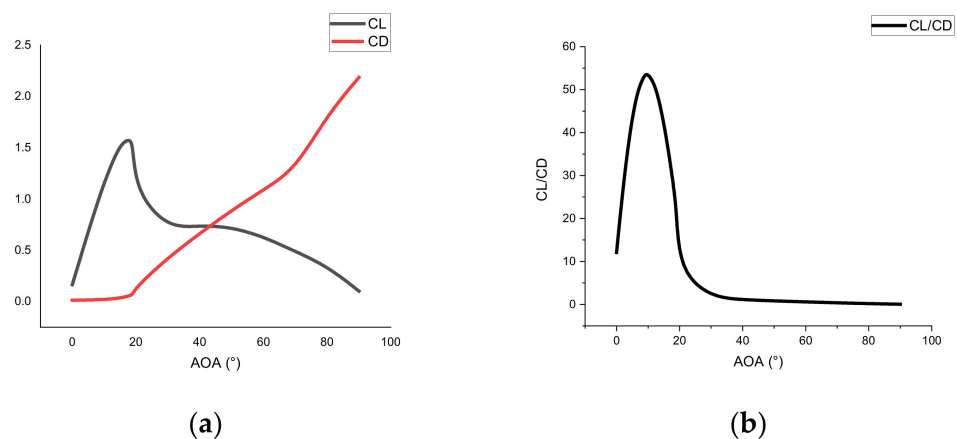

(a) **(b)**

Figure 4. NACA 4415 airfoil aerodynamic performance: (**a**) lift and drag; (**b**) lift—to—drag ratio.

A rough estimation of the initial shape using the panel method or vortex lattice method. CFD tools, such as ANSYS FLUENT, STAR-CCM+, Open Foam, and Abaqus, can be used to refine aerodynamic results in the final stage.

2.2.2. Tradeoffs of Control Surfaces

There are two options regarding whether to set the control surfaces. The first is to keep the control surfaces, which is mainly used in cruise flights and does not utilize the differential torque of the rotor. The second is to cancel the control surfaces, where control torque is generated by the differential torque of the rotor. We opted for a hybrid design, keeping the control surfaces and using the rotor differential torque to better stabilize aircraft simultaneously. Compared to traditional fixed-wing design methods, the control surface area of TW10 is smaller to reduce its impact on overall aerodynamic performance. The aileron area accounts for 12% of the total wing area and their deflection range was from $-30°$ to $30°$. The position of aileron should be arranged in the propeller slipstream area to provide sufficient control torque of the yaw channel in VTOL mode.

2.2.3. CFD Analysis Results

The mature commercial Fluent software Ansys was used to compute aerodynamic coefficients for the speed 20 m/s and the AOA ranges from $0°$ to $90°$. The reason why we chose 20 m/s as the inflow speed is that the UAV users usually carry out aerial photography tasks around 20 m/s. Structured grids are used for computation and the grids near the surfaces are encrypted, with a total number of grids of 3.3×10^6. Grid independence verification has been conducted. With regards to boundary condition, velocity inlet, pressure outlet, and nonslip wall surface are set. $SST\ k - \omega$ turbulence model and pressure-based coupled algorithm are used. In addition, the density of air and inflow velocity are constant. Coupling algorithm selection used second-order upwind scheme. In order to reduce computational complexity, the XOZ plane was set as the symmetrical plane.

The aerodynamic coefficient results, including the lift, drag, and pitch moment coefficients and lift-to-drag ratio, are briefly summarized in Table 2, which summarizes the partial outcomes. Figure 5a,b shows that the maximum lift-to drag ratio was 14.2421. Figure 6a,b gives the velocity magnitude contour at different locations along the wing span under the condition of 20 m/s inflow speed and $6°$ AOA. The maximum speed point always appears at the leading edge of the wing. The maximum lift–drag ratio was not high enough because a compromise was made in order to install a five-lens tilt camera to carry out aerial photogrammetry tasks. The bulge of the lower wing surface affects the aerodynamic performance to a certain degree. The pressure coefficient contour of TW10 is shown in Figure 7. The negative pressure area is concentrated on the leading edge of the upper wing upper surface.

Table 2. Results of aerodynamic coefficients including lift, drag, pitch moment coefficient, and lift-to-drag ratio.

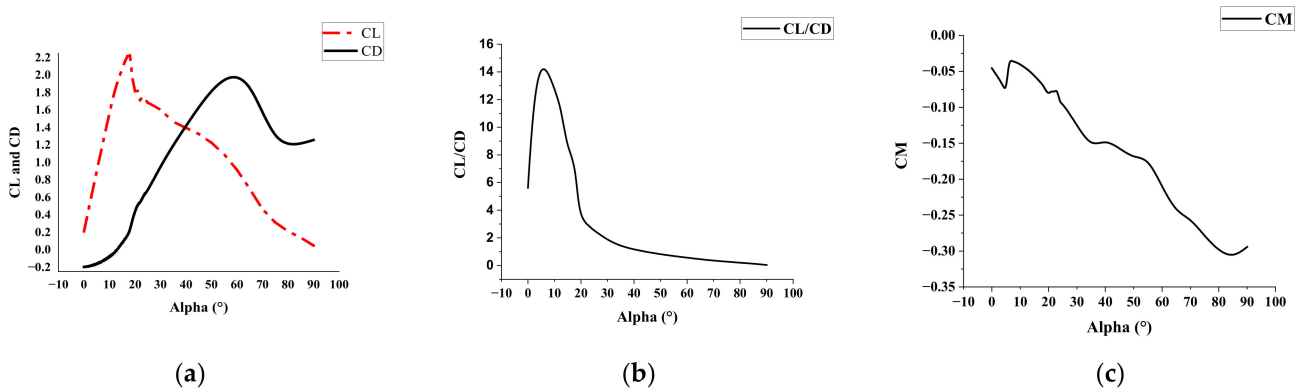| Case	AOA	CL	CD	CM	CL/CD
1	0	0.2107	0.0375	−0.0346	5.6235
2	2	0.4841	0.0439	−0.0366	11.0231
3	4	0.7586	0.0555	−0.0404	13.6629
4	6	1.0212	0.0724	−0.0457	14.2421
5	8	1.3000	0.0947	−0.0524	13.7251
6	10	1.5611	0.1224	0.0603	12.7525
7	12	1.8072	0.1565	−0.0690	11.5499
8	14	1.9948	0.2080	−0.0815	9.5908
9	16	2.2145	0.2645	−0.0790	8.1390
10	18	2.2249	0.3377	−0.0945	6.6890
11	20	1.8155	0.4942	−0.1249	3.6739

Figure 5. CFD results of TW10: (**a**) lift and drag coefficient; (**b**) lift–drag ratio; (**c**) pitch moment coefficient.
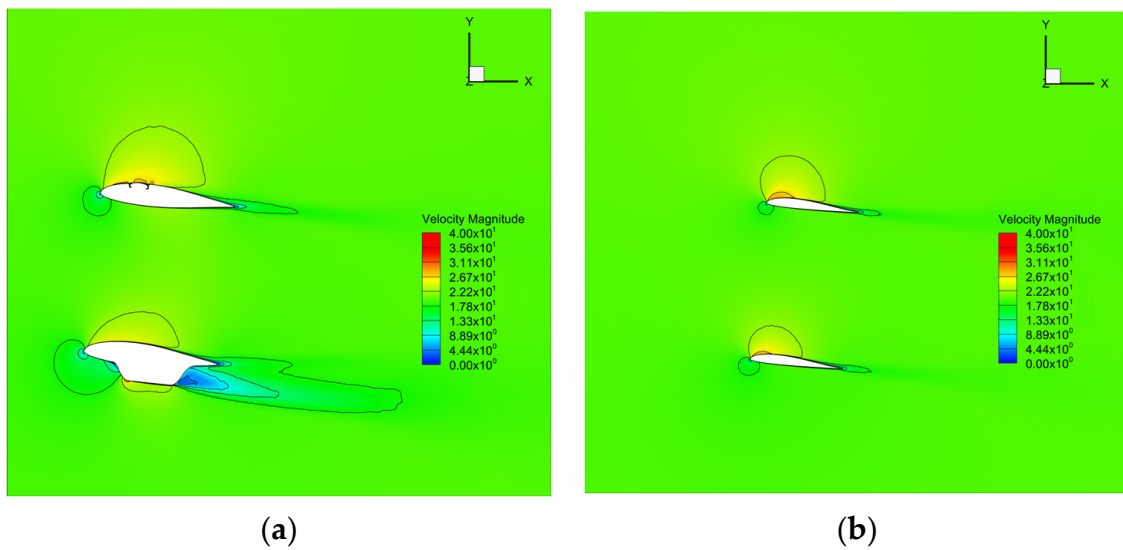

Figure 6. Velocity magnitude contour with 20 m/s speed and 6° AOA: (**a**) X–Z symmetry plane; (**b**) wing tip.
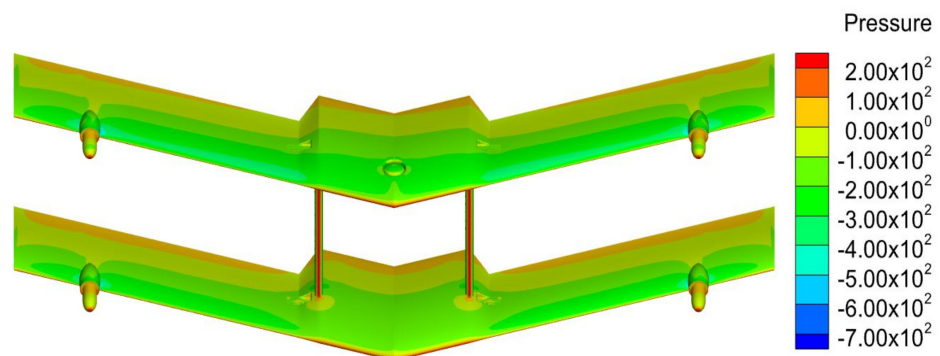

Figure 7. Pressure coefficient contour with 20 m/s speed and 6° AOA.

Aerodynamic analysis presented the following characteristics:

(1) TW10 can provide a maximum lift of more than 10 kg, which ensures safety for transition flight. The maximum lift–drag ratio occurs at a 6° AOA. The CL/CD during the 4~12° angle of incidence is relatively high within the operation point and should be placed.

(2) The pitch-down moment of TW10 is unable to balance naturally according to Figure 5c. Obviously, there is no point where the pitch moment coefficient is 0 from 0° AOA to

90° AOA. Collective elevator deflection or the differential thrust of motors needs to compensate the pitch-down moment.

(3) The fuselage of TW10 contributes approximately 22% of the total lift, while the wings contribute 78%. This proves that the BWB technique is feasible for tail-sitter UAVs.

2.3. Structure, Propulsion, Avionics Design, and Cost Verification

2.3.1. Structure Design and Verification

At present, the skin materials of small UAVs are mostly composed of epoxy-resin-based carbon fiber, adopt a foam sandwich structure, and use basswood wood or carbon fiber for the wing ribs. In this paper, a process plan was designed for the above materials: the mold was produced according to the aerodynamic shape of the aircraft, the carbon fiber cloth was laid by the composite material hand lay-up process, and then the resin was solidified by an autoclave or an oven. The surface machining error of the metal mold was controlled within 0.05 mm in order to guarantee airfoil accuracy and the autoclave used for resin solidification was capable of manufacturing aircrafts with a 2 m wing span.

The wing structure consisted of front beams, rear beams, and ribs. The front beam and rear beam had cross-sections 10 mm in diameter and 6 mm in diameter, respectively. The ribs made of wood were 3 mm thick. The wing skin used a sandwich structure consisting of one layer of foam and two layers of carbon cloth. These parts were glued together with wing skin using special glue. Finally, the estimated weight including all structure components was 1.82 kg.

To verify the structural strength and inertia of TW10 in VTOL mode and forward flight mode, we established a three-dimensional model and carried out static finite element analysis through ANSYS while overloading factor was set to 4 and safety factor was set to 1.2. The specification of carbon fiber cloth is T300. The mechanical property of T300 and ribs are acquired by the manufacturer. The metal parts of TW10 are made of 6061-T651 aluminum alloy.

The connection relationship among all components is set to be bonded. The inertial release method is adopted to solve the statics analysis of the structure in free state. However, the mechanical property of glue between ribs and wing skin is hard to obtain. Thus, the glue used in composite material UAV shell is omitted. The gravity of motor and thrust is modeled as a point force. Aerodynamic lift is considered as uniform load applied to wing skin. Similarly, drag is also applied according to the aerodynamic analysis result. The analysis result of stress and strain is shown in Figures 8 and 9. Stress and strain of all parts is within material strength criterion. In the VTOL mode, the maximum deformation and strain occurs at the motor seat, 1.6 mm and 9.24 MPa. The reason for the large deformation at this location is the large thrust of motors in the VTOL mode and the presence of stress concentration at this area. In the forward flight mode, the maximum deformation occurs at the wingtip, 8.741 mm. The maximum strain occurs near the installation position of photoelectric load, 1.236 Mpa. The ratio of maximum deformation at wingtip to wingspan is 0.437%, which is far lower than 5%. No wing flutter issues occur during whole flight. The geometrical and inertia parameter of TW10 is listed in Table 3.

Table 3. TW10 parameters.

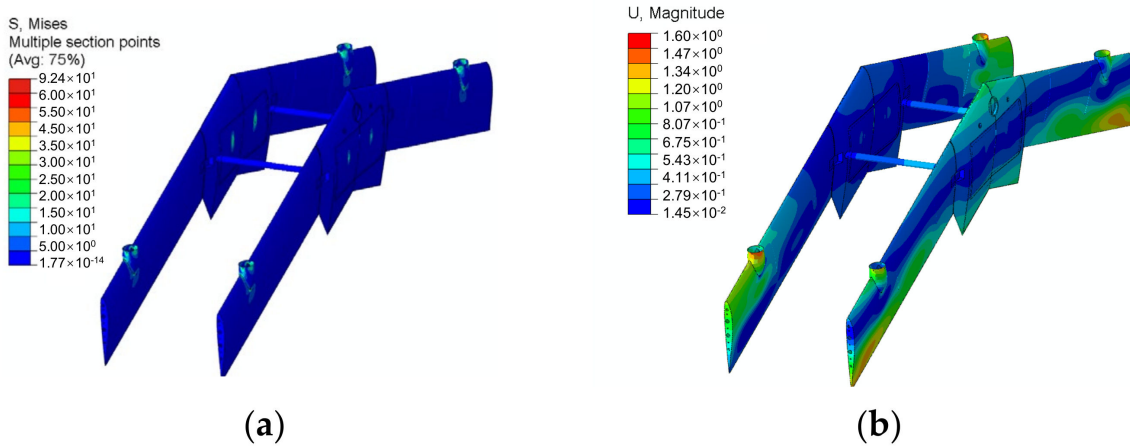| Parameters	Mass	Wing Span	Wing Area (Dual)	Root Chord	Tip Chord	Aspect Ratio
Values	10 kg	2 m	1.32 m^2	0.38 m	0.25 m	7.064
Parameters	X_{cg}	X_{AF}	I_x	I_y	I_z	Sweep angle
Values	0.245 m	0.255	1.524	0.513	1.145	20°

Figure 8. Stress and strain in VTOL mode: (**a**) stress; (**b**) strain.
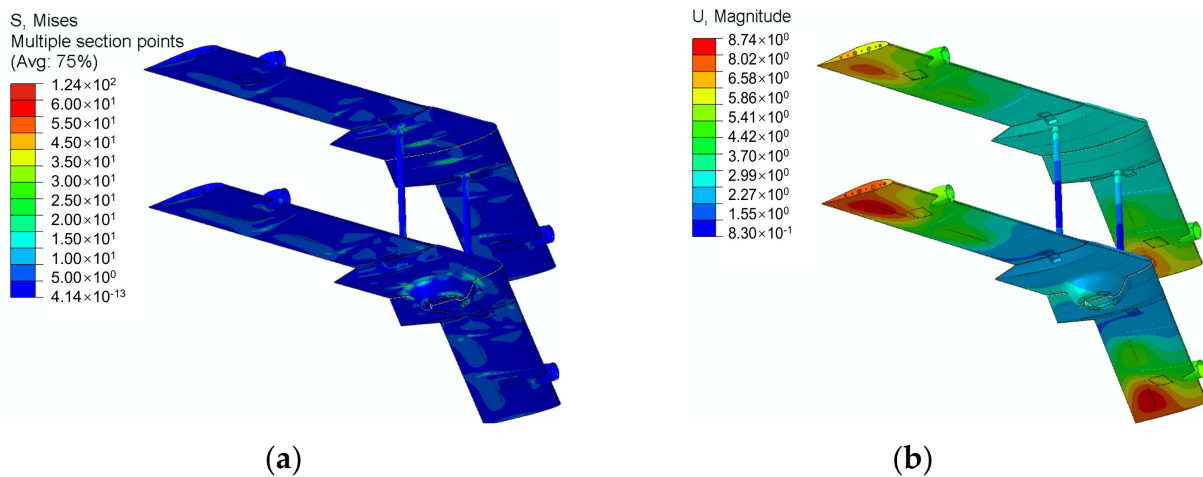

Figure 9. Stress and strain in forward flight mode: (**a**) stress; (**b**) strain.

2.3.2. Propulsion System

When choosing a propulsion system, four aspects require attention. Firstly, different demands are placed on the propulsion system in VTOL mode and forward flight mode. In VTOL mode, larger diameter and small pitch propeller with a higher rotor speed is favored but as for forward flight mode, a small paddle diameter with a larger pitch is required. It is necessary to make a trade-off between these preferences. Secondly, it is common for the thrust of the propeller to decrease as the advance ratio increases; thus, the thrust decreasing amount should be considered. Thirdly, the match between motor and propeller must be considered. Fourthly, the propeller system should provide enough lift in VTOL mode and transition phase so that the thrust-to-weight ratio is greater than 1, while 1.5 may be a suitable option.

To enhance control authority, we adopted a biplane quadrotor configuration. The combination of deferential torque among quad rotors and four ailerons could provide sufficient control torque during full envelope flight. The details of this configuration are discussed in Section 3.

2.3.3. Avionics

The autopilot program used open-source ground station Mission Planner software. The mavlink communication protocol provided air-to-ground transmission of data, including battery voltage, aircraft attitude, position, way-point planning information, remote control states, etc. A long-distance data transmission device was used to ensure flight safety.

The telemetry module pairs operation at 915 Mhz with a communication distance of up to 10 km in real flight tests.

The hardware of the controller was the self-developed flight control board CGBX-V1 with a core processor STM32H743 equipped with triple redundancy inertial measurement units (IMUs), including ADIS16475, BMI088, ICM20649, RM3100 compass, and MS5611 barometer. A pitot tube was used to measure airspeed. If there are many burrs in airspeed data, a filter can be considered, but the filter bandwidth needs to be carefully selected. A propulsion system with Sunny-Sky x3126 motors and APC 1365 propellers was used. APC 1365 may not be the optimal option, but it was sufficient to support the current work. A total of 87,300 mAh 11.2 V batteries provided sufficient power supply for longer flight endurance, and every two 3S batteries were connected in series as a 6S battery because of the cramped space in the wing. The maximum thickness of fuselage limited the battery selection. There was another option for selecting battery packs, which was to use a set of batteries with high discharge rates in the VTOL phase and a set of batteries with low discharge rates in the cruise phase. Under the same energy density conditions, a battery pack with a low discharge rate is lighter. With respect to servo precautions, the servo signal line is often close to the motor power supply line and it is necessary to choose a servo with strong anti-interference ability or to shield the cable.

2.3.4. Cost Verification

The detailed cost accounting process should start after the structural design verification is completed, including raw material costs, equipment costs, energy costs, labor costs, mold costs, component processing costs, production site rental expenses, electronic component procurement costs, etc. It is necessary to negotiate with suppliers to minimize procurement prices based on expected production capacity. For startups, this is a trivial but extremely challenging task.

2.3.5. Prototype

The design parameter specifications of the TW10 prototype are shown in Figure 10 and Table 4, and the design highlights of TW10 are briefly summarized.

Figure 10. TW10 prototype.

Table 4. TW10 weight parameters.

Parameter	Value
Composite fiber body mass	1.8 kg
Wing span	2 m
Power system	1 kg
Battery *	3.26 kg
Height	0.56 m
Width	0.44 m

* Note that 8 3S 7300 mAh batteries equal to 4 6S 7300 mAh batteries.

- Systematic design methods were used to accelerate the development process of the tail-sitter UAV.
- Aerodynamic coefficients over a wide AOA range were evaluated to achieve stable flight in multiple modes.
- The control combination of differential rotor thrust and aerodynamic surface deflection is to ensure effective and safe flight in the full envelope.
- The structure of the UAV was reduced as much as possible, and the weight layout of the cabin was reasonably optimized to ensure that the center of gravity was approximately within the XY plane of the UAV.

3. Dynamics Modeling

In this section, we describe the kinematic and dynamic modeling of the TW10. In order to improve the accuracy of the controller design, we will try to consider rotor dynamics and aerodynamic rudder surface dynamics.

3.1. Strategy of Control

Tail-sitter UAV operates in three flight modes: VTOL mode, transition mode, and forward flight mode, shown in Figure 11.
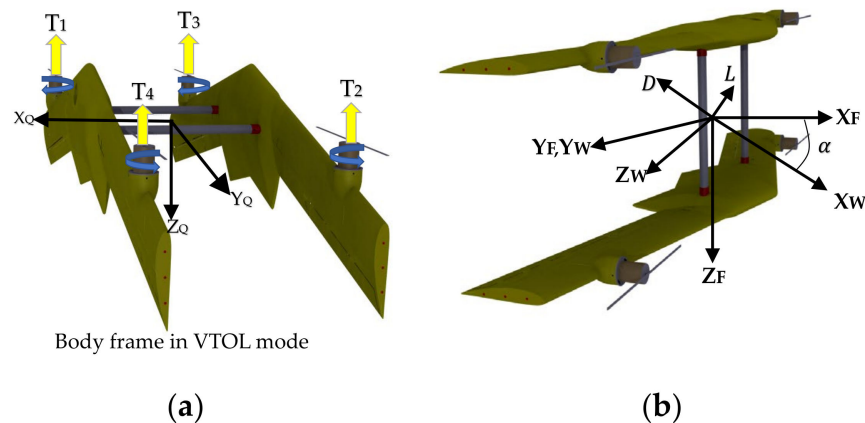

Body frame in VTOL mode

(**a**)   (**b**)

Figure 11. Co-ordination of TW10: (**a**) Subscript Q denotes body frame in VTOL mode; (**b**) Subscript F denotes forward flight body frame while subscript W denotes airflow frame in forward flight mode.

In VTOL mode, vertical movement is completed by increasing/decreasing collective thrust of all the rotors. Pitch motion is achieved by providing differential thrust between upper rotors 2, 3 and lower rotors 1, 4 and the collective deflection of four ailerons. Roll motion is achieved by providing differential thrust between left rotors 1, 2 and lower rotors 3, 4. Yaw motion is achieved by providing deferential deflection between the left and right ailerons instead of the propeller moment produced by the diagonal rotors.

In transition mode, ensuring attitude is under control at a high angle of attack and at a low airspeed and speed up to cruise speed is the most important issue to be handled. The velocity channel is typically modeled as a first- or second-order system for control and thrust curve should be well designed to provide enough lift to conquer the lack of wing lift and meet speed demands. In this paper, transition angle rate is set to constant and there is no limitation in height change. The amount of height change during conversion depends on the design of the throttle curve.

In fixed-wing mode, the pitch control scheme is the same as that in VTOL mode. The roll control scheme corresponds to the yaw channel in VTOL mode. The yaw control scheme corresponds to the roll channel in VTOL mode. The difference in cruise flight between TW10 and traditional fixed-wing aircraft is that TW10 introduces extra moments by deferential thrust. This greatly enhances the attitude control ability in fixed-wing mode, eliminates the possibility of stalling, and enables it to maneuver at any AOA.

3.2. Vehicle Equation of Motion

A mathematical model of biplane-quadrotor tail-sitter UAV in the body axis can be derived by fixing the right-hand co-ordinate axis with respect to conventional wing frame.

3.2.1. Co-ordinate Frame

The co-ordinate of the body frame used in TW10 follows the same structure as the quadrotor in VTOL mode and is consistent with a conventional fixed wing in forward flight mode. The local north-east-down (NED) co-ordinate is chosen as the inertial frame, as shown in Figure 11a,b.

3.2.2. Flight Dynamics

In order to design the TW10 control system, the force equation, moment equations, and kinematic equations were deduced.

Force equation:

$$
\begin{bmatrix} \dot{u} \\ \dot{v} \\ \dot{w} \end{bmatrix} = \begin{bmatrix} 0 \\ 0 \\ -\frac{T}{m} \end{bmatrix} + \begin{bmatrix} \frac{F_{ax}}{m} \\ \frac{F_{ay}}{m} \\ \frac{F_{az}}{m} \end{bmatrix} + g \begin{bmatrix} 2\eta_1\eta_3 - 2\eta_0\eta_2 \\ 2\eta_1\eta_3 - 2\eta_0\eta_2 \\ \eta_0^2 - \eta_1^2 - \eta_2^2 + \eta_3^2 \end{bmatrix} + \begin{bmatrix} rv - qw \\ pw - ru \\ qu - pv \end{bmatrix} \tag{1}
$$

Moment equation:

$$
\begin{bmatrix} \dot{p} \\ \dot{q} \\ \dot{r} \end{bmatrix} = \begin{bmatrix} (c_1 r + c_2 p)q + c_3\overline{L} + c_4 N \\ c_5 pr - c_6(p^2 - r^2) + c_7 M \\ (c_8 p - c_2 r)q + c_4\overline{L} + c_9 N \end{bmatrix} \tag{2}
$$

$$
\begin{bmatrix} c_1 \\ c_2 \\ c_3 \\ c_4 \\ c_8 \\ c_9 \end{bmatrix} = \Lambda \begin{bmatrix} (I_y - I_z)I_z - I_{xz}^2 \\ (I_x - I_y + I_z)I_{xz} \\ I_z \\ I_{xz} \\ I_x(I_x - I_y) - I_{xz}^2 \\ I_x \end{bmatrix}, \Lambda = \frac{1}{(I_x I_z - I_{xz}^2)} \tag{3}
$$

$$
\begin{bmatrix} c_5 \\ c_6 \\ c_7 \end{bmatrix} = \frac{1}{I_y} \begin{bmatrix} (I_z - I_x) \\ I_{xz} \\ 1 \end{bmatrix} \tag{4}
$$

3.2.3. Kinematics

Due to the flight characteristics of the tail-sitter UAV, the kinematic equation can be expressed in quaternion as:

$$
\begin{bmatrix} \dot{\eta}_1 \\ \dot{\eta}_2 \\ \dot{\eta}_3 \\ \dot{\eta}_4 \end{bmatrix} = \frac{1}{2} \begin{bmatrix} -\eta_1 & -\eta_2 & -\eta_3 \\ \eta_0 & -\eta_3 & \eta_2 \\ \eta_3 & \eta_0 & -\eta_1 \\ -\eta_2 & \eta_1 & \eta_0 \end{bmatrix} \begin{bmatrix} p \\ q \\ r \end{bmatrix} \tag{5}
$$

Let the position be $p = (x, y, z)^T$ in the earth frame and the velocity be $v = (u, v, w)$ in the body frame, the equation is:

$$
\dot{p} = R_{BE}(\eta)v \tag{6}
$$

where:

$$
R_{BE}(\eta) = \begin{bmatrix} \eta_0^2 + \eta_1^2 - \eta_2^2 - \eta_3^2 & 2\eta_1\eta_2 - 2\eta_3\eta_0 & 2\eta_1\eta_3 - 2\eta_2\eta_0 \\ 2\eta_1\eta_2 + 2\eta_3\eta_0 & \eta_0^2 - \eta_1^2 + \eta_2^2 - \eta_3^2 & 2\eta_2\eta_3 - 2\eta_0\eta_1 \\ 2\eta_1\eta_3 - 2\eta_2\eta_0 & 2\eta_2\eta_3 + 2\eta_1\eta_0 & \eta_0^2 - \eta_1^2 - \eta_2^2 + \eta_3^2 \end{bmatrix} \tag{7}
$$

3.2.4. Wing Aerodynamic

Because the gap-to-chord ratio was set as 2, we ignored the aerodynamic interference between the upper wing and lower wing. The aerodynamic model should be considered for full flight envelope since the lift, drag, and pitch moment change dramatically when the UAV experiences a large pitch angle and simultaneously increases the horizontal speed. Lift and drag forces can be calculated by:

$$
\begin{aligned}
L &= \tfrac{1}{2}\rho V^2 S C_L(\alpha) \\
D &= \tfrac{1}{2}\rho V^2 S C_D(\alpha)
\end{aligned}
\tag{8}
$$

where ρ is the density of air, V is the inflow speed, S is the wing area, and C_L and C_D are the corresponding lift and drag coefficients, respectively, at the certain (AOA) α. The AOA is defined by $\alpha = \frac{arctanW}{U}$. The velocities in the body frame U and W can be calculated by the co-ordinate transformation of the inertial frame speed. For the aerodynamic model in this study, the data of lift and drag coefficient versus AOA can be acquired from CFD results, which are illustrated in Figure 5. Airfoil shape accuracy and surface roughness were guaranteed by the aircraft metal molds.

The prop-wash effect plays a significant role in the hover stage and transition stage. Thus, it is necessary to evaluate the influence of prop wash. In this paper, wing area was divided into prop-wash area and non-prop-wash area. It was assumed that the prop wash of the propeller only affected the lift by generating induced velocity. The propeller-wash effect can be evaluated by the following formula:

$$
V_{flow} = \sqrt{V_{inflow}^2 + \frac{2T_{prop}}{\rho D_p}}
\tag{9}
$$

where D_p is diameter of the propeller, T_{prop} is the thrust of the propeller, ρ is the air density, and V_{inflow} is the inflow wind speed.

3.2.5. Propeller Model and Measurement

In order to acquire the static thrust performance in VTOL mode of the APC 1365 propeller with the Sunny-Sky x3126 motor, which is produced by zhongshan sunny-sky Model Co., Ltd., China, an electric propulsion test bench shown in Figure 12a is purchased, which consists of electronic speed control (ESC), force sensor, rpm sensor, controller, and torque sensor. The thrust force increased with the increase in rotating speed per minute (RPM). Static thrust test bench and thrust test results are shown in Figure 12b.
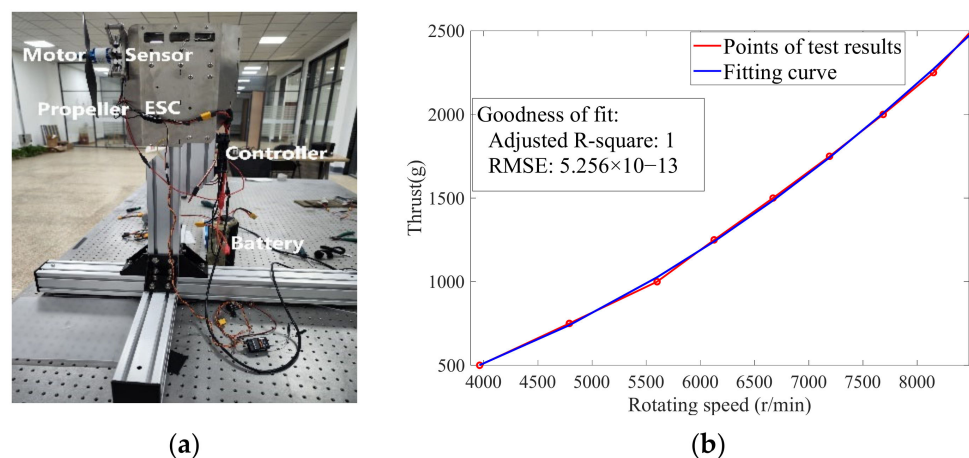

Figure 12. Static thrust test bench and thrust test result. (**a**) Test bench; (**b**) fitting curve.

In the past decades, the research on quadrotor UAV has become relatively established. However, due to the low forward flight speed of multijrotor UAV, less attention has been

paid to the aerodynamic performance of the propeller at a certain inflow speed. Upon detailed tests, it was found that the efficiency of the propeller decreased at higher inflow speeds. Aiming to evaluate the performance of the propeller under incoming flow, we tested the propeller both in static environments and in the wind tunnel at the China Aerospace Aerodynamics Research Institute Harbin, Heilongjiang Province.

Since TW10 is a product that is still in the early stages of development, it was unrealistic to design and manufacture the propeller independently. Because of the long research and development cycle and high costs, it is difficult for startups to gain approval for small batch production. Thus, we initially used commercial APC series made in USA at first. Wind tunnel tests were carried out with Sunny-Sky x3126 motor accompanied with APC 1365 and APC 1280 propellers, respectively. A test bench is well designed for dynamic thrust tests and consists of a frame made of aluminum alloy, an rpm sensor, an ammeter, a force sensor, a battery, and an ESC. The test bench tested in the wind tunnel is shown in Figure 13.
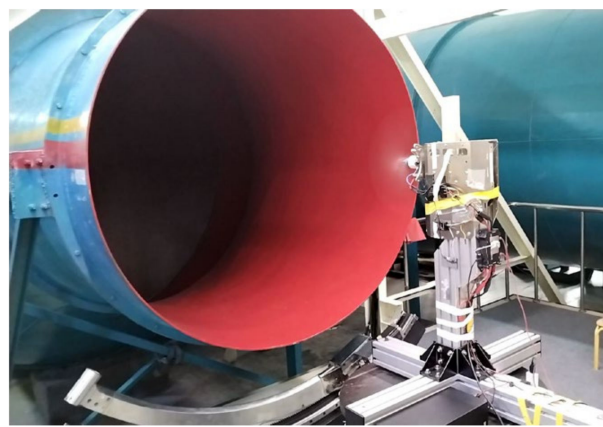
Figure 13. Dynamic thrust test bench.

The size of the wind tunnel was 1 m×1 m, and the incoming wind speed varied from 0 m/s to 30 m/s. The test data are shown in Figure 14a,b. Although the applied sensor had a certain constant error due to the additional windward area of test bench, the data were still able to reflect the changing trend. Ranging from 0 m/s to 30 m/s wind speed, the power efficiency of the propeller decreases significantly. The APC 1365 propeller has better efficiency at cruise speed.
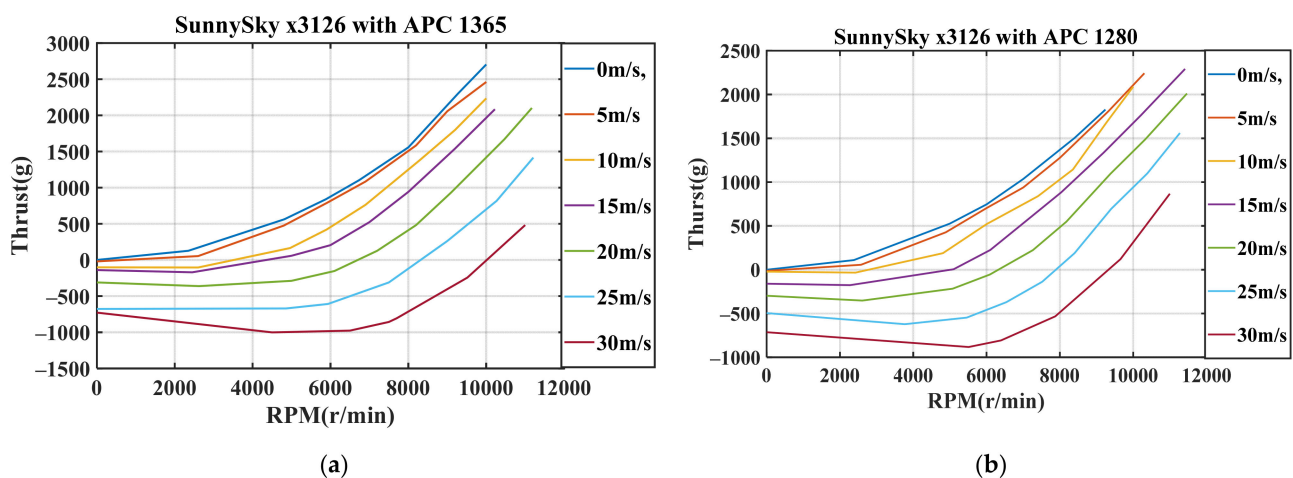

(**a**)

(**b**)

Figure 14. Dynamic thrust test results of Sunny-Sky motor: (**a**) Sunny—Sky x3126 with APC 1365; (**b**) Sunny-Sky x3126 with APC 1280.

The thrust exerted by the propeller can be obtained by:

$$T = \rho D_p^4 C_T \left(\frac{N}{60} \right)^2 \tag{10}$$

where D_p denotes the diameter of the propeller, C_T and C_M are dimensionless coefficients representing thrust and torque, and N denotes the RPM. D_p and ρ are constants when flying at low altitude.

From the test data, we deduce the rule that, with the increase in the advance ratio, the efficiency of the power system decreases. The larger the diameter of the propeller disc, the greater the drop. The larger the propeller pitch, the smaller the drop. Thus, it is necessary to choose the appropriate small disc diameter and large pitch propeller. The coefficient C_T can be simplified as a linear function of the advance ratio.

$$C_T = k1J + k2 \tag{11}$$

where $J = \frac{V_{inflow}}{ND_p}$ is the advance ratio and $k1$ and $k2$ are constant. N is rotor speed per minute, V_{inflow} is the inflow wind speed, and D_p is the diameter of the propeller.

Substituting Equation (11) into Equation (10):

$$T = \rho D_p^4 (k1J + k2) \left(\frac{N}{60} \right)^2 \tag{12}$$

4. Controller Design

This chapter divides the controller design process into three parts according to the control modes: VTOL controller design, transition controller design, and forward flight controller design. In VTOL controller design, cascaded PID controller is employed for the prototype verification.

4.1. VTOL Attitude Control Base

In this study, the attitude controller consisted of an outer loop and inner loop. The outer loop was an angle loop and the inner loop was an angular rate loop. An L1 adaptive controller was used in the inner loop [26], which was not repeated in this paper. The velocity controller and height controller adopted a single loop structure, which is not described in this article. The use of Euler angles in the attitude controller for tail-sitter will lead to singularity in VTOL mode. Thus, we decided to employ the quaternion feedback method to design the controller. Quaternion multiplication is defined as:

$$\overline{\eta_d} = \overline{\eta_e} \bigotimes \overline{\eta_a} = M(\overline{\eta_a})\overline{\eta_e} = \begin{bmatrix} \eta_4 & -\eta_3 & \eta_2 & \eta_1 \\ \eta_3 & \eta_4 & -\eta_1 & \eta_2 \\ -\eta_2 & \eta_1 & \eta_4 & \eta_3 \\ -\eta_1 & -\eta_2 & -\eta_3 & \eta_4 \end{bmatrix} \overline{\eta_e} \tag{13}$$

$$\overline{\eta_e} = M(\overline{\eta_a})^T \overline{\eta_d} \tag{14}$$

where $\overline{\eta_d}$ denotes the desired attitude angle; $\overline{\eta_a}$ is the actual attitude provided by the attitude and heading reference system and $\overline{\eta_e}$ is the difference between the desired attitude and actual attitude.

4.2. Transition Attitude Control

In our tests, the transition maneuver from VTOL mode to forward flight mode was apt to air crashes. The transition phase is a bridge connecting VTOL mode and forward flight mode. A constant pitch angle rotating rate has been set and its value depends on the match between propulsion system and body mass. A large thrust–weight ratio responds to fast rotation. For TW10, rotating rate is set to 15 deg/s. The control strategy is to control the

aircraft near the stall angle in VTOL mode and switch to forward flight mode. During the transition to forward flight mode, the lack of lift due to the low airspeed is compensated by component force of rotor thrust. The thrust gradually decreases with the increase in the transition angle, and the airspeed gradually increases with the increase in the rotating angle. The matching of thrust and airspeed is the most critical point in transition. The aerodynamic lift and drag coefficient provide design basis for thrust curve.

The transition from forward flight mode to VTOL mode is relatively safe; thus, we do not address it further in this paper.

4.3. Forward Flight Attitude Control Based on Cascaded PID Control

Considering that the cruise phase was less disturbed, traditional cascade PID control was introduced. The PID controller is convenient to tune and easy to implement.

Figure 15 shows the structure of the controller. The total energy control system is applied as a speed and height controller, which generated the throttle and pitch command to the attitude loop. The L1 navigation controller provided yaw and roll command. It is vital to highlight that, due to the existence of differential thrust in the pitch channel, it is difficult for tail-sitter UAV to enter into the stall condition.
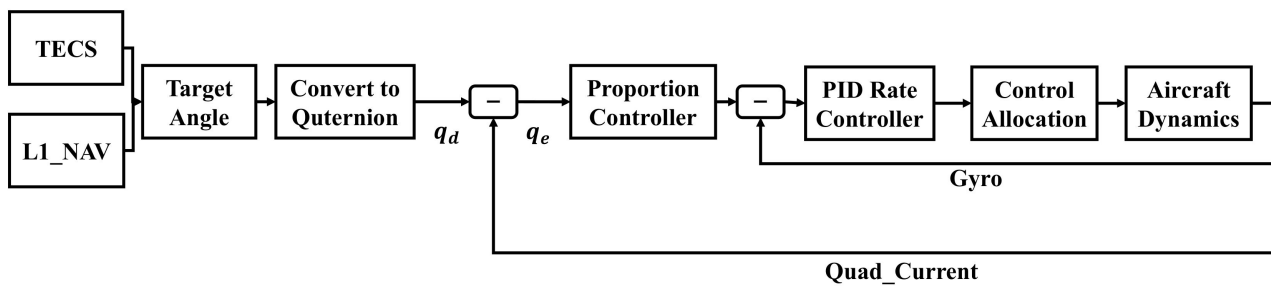
Figure 15. Cascaded PID controller structure.

4.4. Control Allocation

In Section 3.1, we stated that the maneuver difference between VTOL mode and forward flight mode is the swap yaw axis and roll axis. Thus, the expressions of the total forces and moment in VTOL mode are given as:

$$T = T_1 + T_2 + T_3 + T_4 \tag{15}$$

$$M_r = \begin{bmatrix} L_v \\ M_v \\ N_v \end{bmatrix} = \begin{bmatrix} R(-T_1 - T_2 + T_3 + T_4) + C_{l\delta_e}\delta_e \\ P(-T_1 + T_2 - T_3 + T_4) + C_{m\delta_e}\delta_e \\ C_{n\delta_e}\delta_e \end{bmatrix} \tag{16}$$

where R is the roll axis moment arm, P is the pitch axis moment arm, and $C_{l\delta_e}$ is the control derivative of the elevon for the roll axis. $C_{m\delta_e}$ is the control derivative of the elevon for the pitch axis. $C_{n\delta_e}$ is the control derivative of the elevon for the yaw axis.

The expressions for forces and moments in the fixed-wing mode are given as:

$$T = T_1 + T_2 + T_3 + T_4 \tag{17}$$

$$M_r = \begin{bmatrix} L_v \\ M_v \\ N_v \end{bmatrix} = \begin{bmatrix} R(-T_1 - T_2 + T_3 + T_4) + C_{\delta_e}\delta_e \\ C_{\delta_a}\delta_a \\ P(-T_1 + T_2 - T_3 + T_4) \end{bmatrix} \tag{18}$$

5. Simulation and Flight Test Results

5.1. Simulink Simulation

5.1.1. Hover Simulation

All the aircraft parameters were incorporated into the simulation system. The aim of the simulation was to verify the feasibility of full flight envelope controller, especially for the pitch channel. TW10 is commanded to track (x_d, y_d, z_d) from $(0, 0, 0)$ to $(0, 0, 50)$. To test the attitude track performance, a step signal with $10°$ amplitude was added into the pitch channel. The results are shown in Figure 16a. As observed in Figure 16b, TW10 tracked the given way points with an acceptable response.
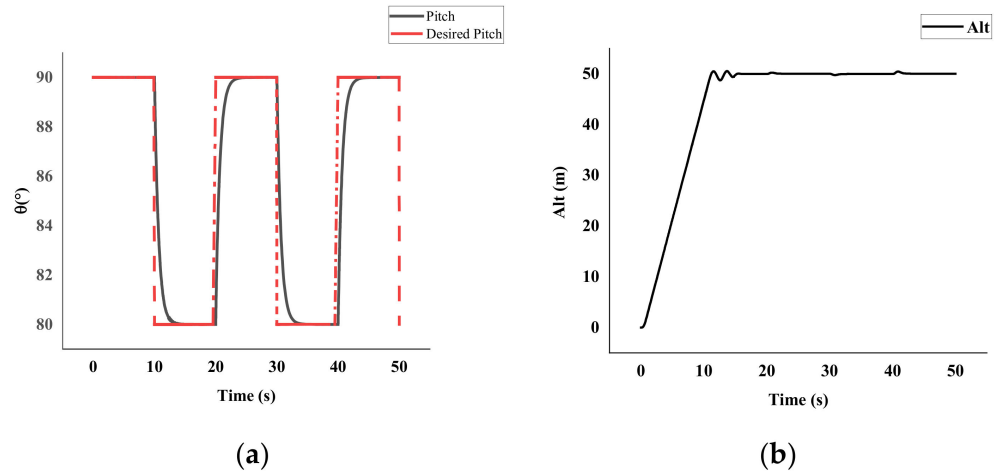
Figure 16. Hover performance. (**a**) Hover pitch attitude; (**b**) hover altitude.

5.1.2. Full Flight Envelope Simulation

TW10 was commanded to takeoff in VTOL mode; the position and attitude is controlled by VTOL controller. When the UAV reaches 50 m altitude, it transitioned to forward flight mode. During the transition process, attitude was still controlled by VTOL controller when the pitch angle is smaller than the switch angle and was controlled by forward flight controller when pitch angle is larger than switch angle. The switch angle was set to $45°$ in this paper.

The full envelope simulation results are shown in Figure 17. Through longitudinal full flight envelope simulation, the feasibility of the proposed algorithm is verified. During the VTOL phase, transition phase, and forward flight phase, vehicle attitude and altitude were acceptable. The transition maneuver occurred at 10.0 s, while transition time was set to 5 s.
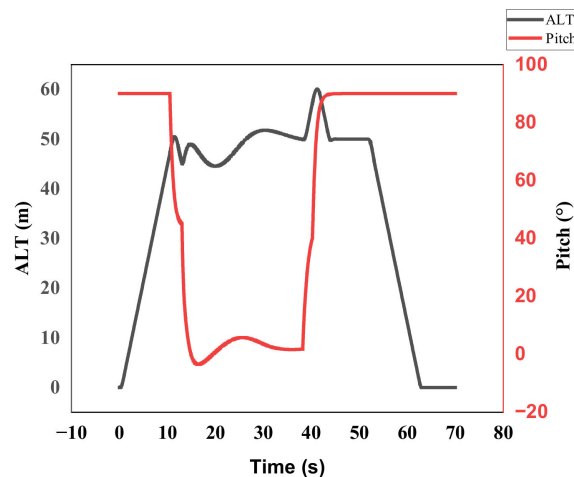

Figure 17. Full envelope simulation result.

5.2. Flight Test Results

(1)   Hover Stage Test

The flight test was divided into two parts. The first part tested the hovering stability, and the aircraft was most affected by wind disturbance during the hovering phase. Hovering experiments were conducted both in windy and non-windy environments, respectively. The results of the hovering experiment with wind are shown in Figure 18. Test result in the windy environment had a 4 m/s wind speed. It is observed that controllers can achieve relatively good hovering, while experimental data are shown in Figure 19.

(**a**)   (**b**)
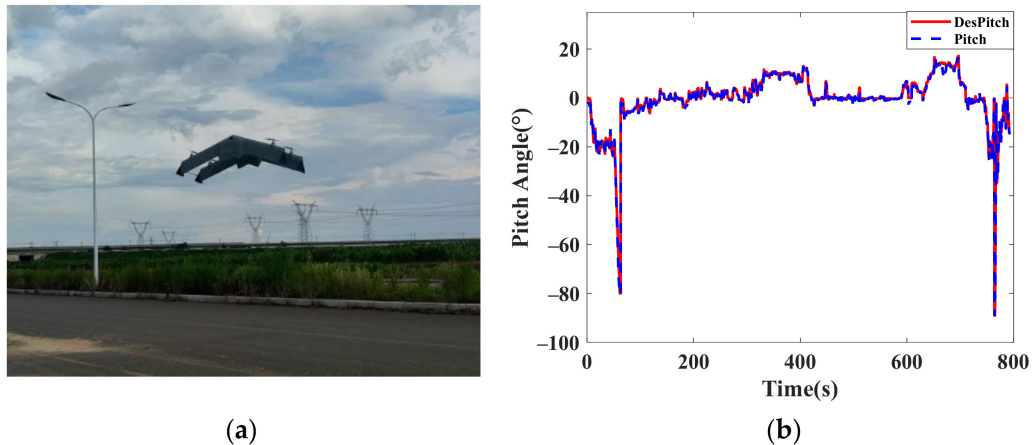
Figure 18. Outdoor hover flight test results: (**a**) hovering test; (**b**) hover pitch angle.

(**a**)   (**b**)

Figure 19. Outdoor manual flight: (**a**) level flight; (**b**) transition.

(2)   Full Envelope Manual Flight Test

The second part was the manual flight and autonomous full envelope flight test. Flight photos are shown in Figure 19. The local wind speed was approximately 10 m/s. The first flight of TW10 under manual pilot control was carried out, aiming to verify whether the technical solution is correct. For the cruise flight phase in 40–750 s, the response of attitude is shown in Figure 20a,b. Flight trajectory is shown in Figure 20c.
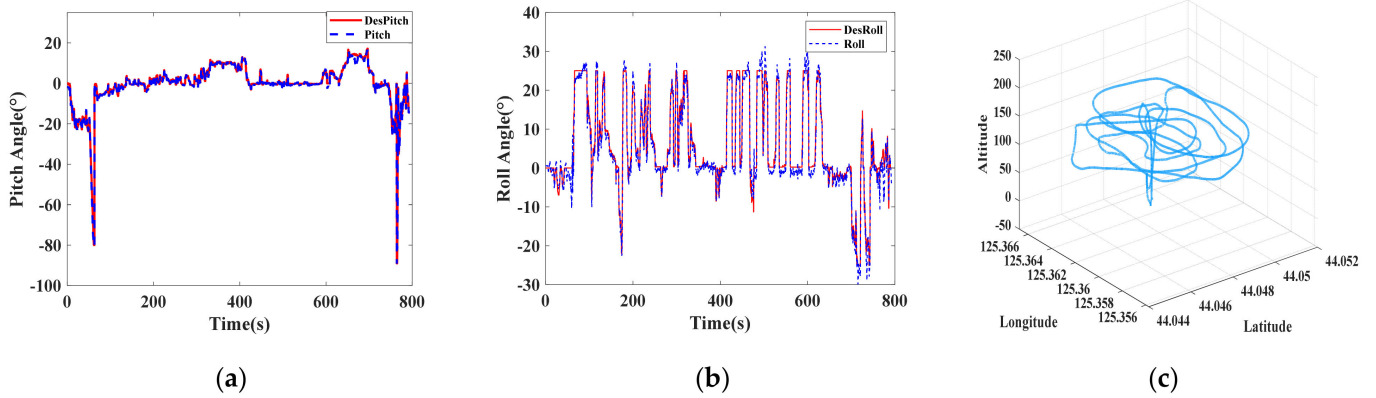
Figure 20. Outdoor manual flight attitude tracking results: (**a**) pitch angle, (**b**) roll angle, and (**c**) trajectory.

After the success of the manual test, outdoor autonomous flight test needed to be carried out. The pitch and roll angles are shown in Figure 21a,b. The pitch channel realized satisfactory performance with a 0.5° track accuracy. There are small oscillations with a 1.5° amplitude in the roll channel due to the structure dead zone of the elevon. In this test, the wind speed was approximately 5 m/s. The difference between ground speed and airspeed shows the strength of wind speed, which is shown in Figure 22. In order to ensure flight and crew safety, flight route altitude was set to 200 m. The transition begins at 160 m altitude and reaches 202 m after transition progress. In the cruise flight phase, TW10 maintained good attitude accuracy within 1 m and cruise speed stability during wind gust. The average cruise speed was around 13~14 m/s and cruise AOA is 6~7°.
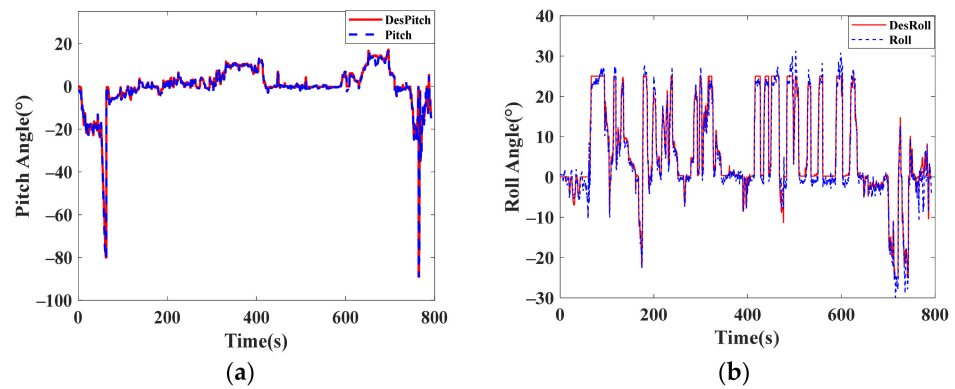
Figure 21. Outdoor autonomous attitude tracking results: (**a**) pitch angle; (**b**) roll angle.
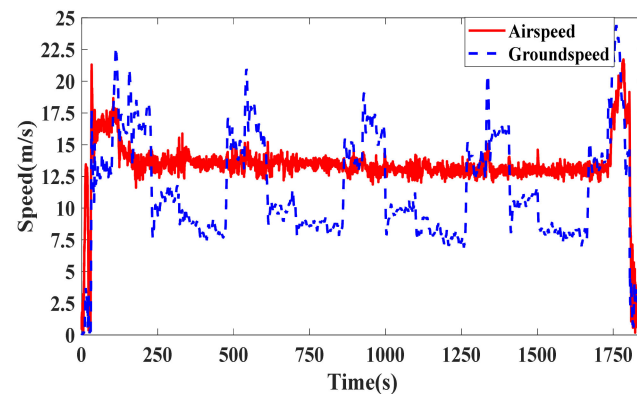

Figure 22. Outdoor autonomous position tracking experiment results.

To prevent the occurrence of stalling during the bank-to-turn (BTT) period, roll angle was limited to 25°. When the aircraft flew downwind, ground speed increased significantly. Thus, the turning radius has also increased, which can be observed in Figure 23a. For the backward transition, transition progress was commanded to finish in 2 s. The kinetic energy is rapidly converted into potential energy. The extent of the post-transition height change was approximately 37 m. If the load on the lower wing is heavy, the back transition rate must be carefully adjusted, otherwise there may be an actuator saturation problem. The altitude track performance is shown in Figure 23b.

(**a**)   (**b**)
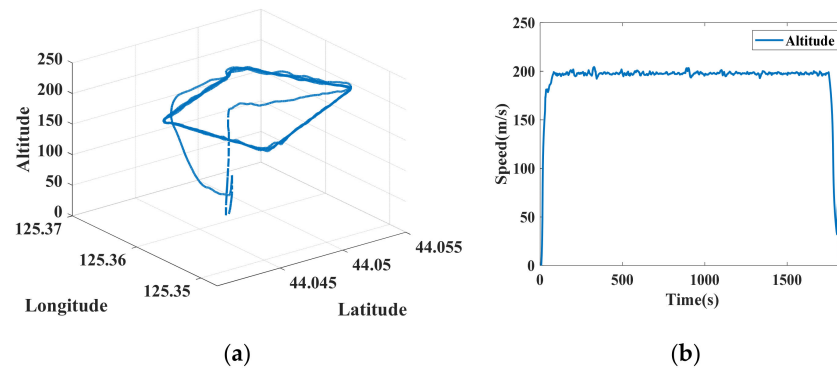
Figure 23. Outdoor autonomous position tracking experiment results: (**a**) trajectory; (**b**) altitude.

With regard to energy consumption aspect, autonomous flight test lasted about 30 min, while power consumption was approximately 5600 mAh, with a 29,200 mAh total battery capacity. The average total current in VTOL mode is 80 A, while 11 A in forward flight mode. The current of the motor is read by a sensor and data were sent to the remote control and ground station. Based on the consumption data, the flight time of UAV under cruise condition would be no less than 2.5 h, which meets the design index requirements. Considering the performance degradation of the battery in extremely cold weather, the flight time in cold regions would be reduced. The power consumption of the motors on the lower wing was slightly higher than that of the motors on the upper wing because lower motors need to provide more thrust than the upper motors to generate pitch trim moment.

After the reliability verification of the performance of TW10, a two-axis infrared dual photothermal imaging gimbal camera pod was installed. The pod was installed with a 640 × 480 high-resolution infrared detector, a 30 times optical zoom full HD visible light camera, and a high-precision gyro stabilized platform. By attaching different photoelectric loads, TW10 could complete various missions, such as reconnaissance, monitor, farmland growth detection, etc. TW10 with load can be seen in the Figure 24a. The photo pictured by the camera is shown in Figure 24b,c.
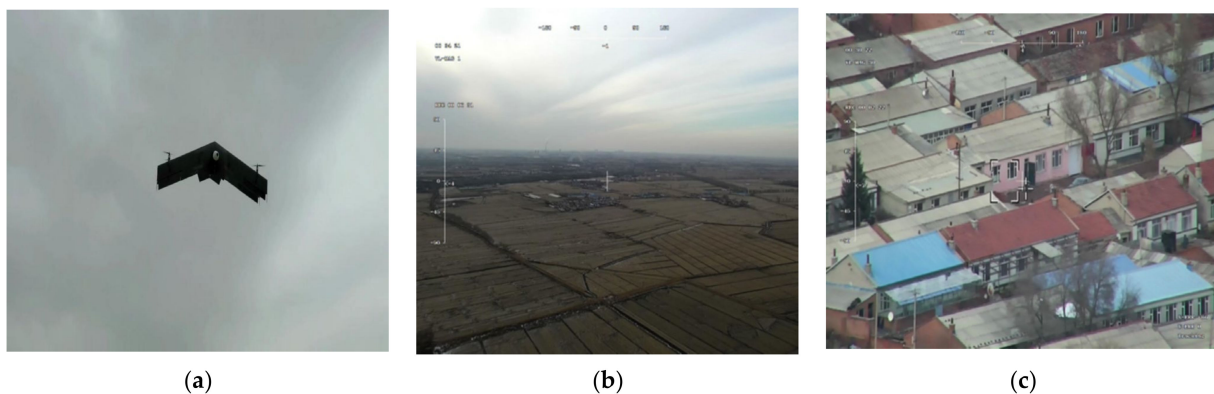

(**a**)   (**b**)   (**c**)

Figure 24. Photoelectric load integration test: (**a**) TW10 with load, (**b**) 1× zoom graph, and (**c**) 30× zoom graph.

6. Conclusions

The tail-sitter UAV is a highly promising type of VTOL UAV. However, due to the two obvious drawbacks in steady transition process and poor wind resistance performance, it has not played its due role in practical scenarios. In this paper, we adopted the blended-wing-body (BWB) technique and biplane quadrotor configuration to design a unique tail-sitter UAV named TW10. The TW10 has a stable transition progress and possesses strong wind resistance capacity. In each design step, we shared special considerations and tackling measures, including aerodynamic compromises, structure design and verification, avionics choices, controller conception, and real flight test.

With regards to aerodynamic design, the most important thing is to choose an airfoil with high lift-to-drag ratio and small pitch-down torque coefficient. Maintaining enough structure stiffness while reducing weight is a thorny problem in structure design. If the stiffness is not enough, the outer wing is easy to flutter during VTOL mode and forward flight mode, which brings annoying noise to sensors. We do not recommend using variable pitch propellers for small UAVs, as they bring high complexity and additional mass. The controller scheme consists of two controllers. An individual VTOL controller and forward flight controller together make up full envelope flight controller. The transition period comprised the linking of the two modes.

Acceptable simulation results and autonomous flight test results proved the success of our first tail-sitter UAV for the commercial market and increased confidence in larger aircraft development. A comparison between our design and actual specifications of TW10 is shown in Table 5, which proves the actual flight performance of TW10 fully meets the design specifications. We believe that tail-sitter UAVs will certainly come to occupy a particular market share in the civil UAV market.

Table 5. Comparation between design and actual specifications.

Design Parameter	Design Value	Actual Value
Max takeoff weight	≥10 kg	≥14 kg
Wing span	≤2 m	2 m
Payload	>1 kg	1.2 kg
Flight endurance	≥120 min	>150 min
Cruise speed	≥13 m/s	14 m/s
Stalling speed	≤12 m/s	11.5 m/s

7. Future Work

In our future work, we will carry out the following tasks:

(1) The structure will be further optimized through joint optimization by Isight, Catia, and ANSYS. Structural quality is the first optimization goal under the premise of ensuring structural rigidity and structural mode.
(2) The controller switchover process needs to be canceled. The feasibility and reliability of the global controller will be verified for the full flight envelope.
(3) Tail-sitter UAV fault reconfiguration control will be explored to improve flight reliability.
(4) It is still necessary to optimize matching between the propeller and the motor, as well as the design of the propeller at different inflow speeds.

References

1. Li, S.; Cummings, M.L.; Welton, B. Assessing the impact of autonomy and overconfidence in UAV first-person view training. *Appl. Ergon.* **2022**, *98*, 103580. [CrossRef] [PubMed]
2. Lozano-Hernández, Y.; Martínez de la Cruz, I.; Gutiérrez-Frías, O.; Lozada-Castillo, N.; Luviano-Juárez, A. Design Procedure of a Low-Cost System for Energy Replenishment in a Quadrotor UAV through a Battery Exchange Mechanism. *Drones* **2023**, *7*, 270.
3. Fu, X.; Jiang, Q.; Yang, X.; Liu, L.; Liu, L.; Li, J.; Li, S.; Luo, Q.; Chen, J.; Zhao, Z.; et al. Nutrients' Removal from Mariculture Wastewater by Algal–Bacterial Aggregates Developed from Spirulina platensis. *Water* **2023**, *15*, 396.
4. La Salandra, M.; Colacicco, R.; Dellino, P.; Capolongo, D. An Effective Approach for Automatic River Features Extraction Using High-Resolution UAV Imagery. *Drones* **2023**, *7*, 70.
5. Li, Z.; Zhang, Y.; Wu, H.; Suzuki, S.; Namiki, A.; Wang, W. Design and Application of a UAV Autonomous Inspection System for High-Voltage Power Transmission Lines. *Remote Sens.* **2023**, *15*, 865. [CrossRef]
6. Sun, J.; Li, B.; Jiang, Y.; Wen, C.Y. A Camera-Based Target Detection and Positioning UAV System for Search and Rescue (SAR) Purposes. *Sensors* **2016**, *16*, 1778. [CrossRef]
7. Michael, N.; Fink, J.; Kumar, V. Cooperative manipulation and transportation with aerial robots. *Auton. Robot.* **2010**, *30*, 73–86. [CrossRef]
8. Li, L.; Zhang, X.; Yue, W.; Liu, Z. Cooperative search for dynamic targets by multiple UAVs with communication data losses. *ISA Trans.* **2021**, *114*, 230–241. [CrossRef]
9. Bai, X.; Yang, M. UAV based accurate displacement monitoring through automatic filtering out its camera's translations and rotations. *J. Build. Eng.* **2021**, *44*, 102992. [CrossRef]
10. Wang, X.; Yuan, X.; Zhu, J.; Yang, Y. Stability Analysis of Tailsitters in Vertical Takeoff and Landing Flights. *J. Aircr.* **2019**, *56*, 1487–1500. [CrossRef]
11. Li, B.; Sun, J.; Zhou, W.; Wen, C.-Y.; Low, K.H.; Chen, C.-K. Transition Optimization for a VTOL Tail-Sitter UAV. *IEEE-Asme Trans. Mechatron.* **2020**, *25*, 2534–2545. [CrossRef]
12. Sridharan, A.; Govindarajan, B.; Chopra, I. A Scalability Study of the Multirotor Biplane Tailsitter Using Conceptual Sizing. *J. Am. Helicopter Soc.* **2020**, *65*, 1–18. [CrossRef]
13. Yao, X.; Liu, W.; Han, W.; Li, G.; Ma, Q. Development of Response Surface Model of Endurance Time and Structural Parameter Optimization for a Tailsitter UAV. *Sensors* **2020**, *20*, 1766. [CrossRef]
14. Yuksek, B.; Vuruskan, A.; Ozdemir, U.; Yukselen, M.A.; Inalhan, G. Transition Flight Modeling of a Fixed-Wing VTOL UAV. *J. Intell. Robot. Syst.* **2016**, *84*, 83–105. [CrossRef]
15. Flores, G.R.; Escareño, J.; Lozano, R.; Salazar, S. Quad-Tilting Rotor Convertible MAV: Modeling and Real-time Hover Flight Control. *J. Intell. Robot. Syst.* **2012**, *65*, 457–471. [CrossRef]
16. Cetinsoy, E.; Dikyar, S.; Hancer, C.; Oner, K.T.; Sirimoglu, E.; Unel, M.; Aksit, M.F. Design and construction of a novel quad tilt-wing UAV. *Mechatronics* **2012**, *22*, 723–745. [CrossRef]
17. Çoban, S. Autonomous performance maximization of research-based hybrid unmanned aerial vehicle. *Aircr. Eng. Aerosp. Technol.* **2020**, *92*, 645–651. [CrossRef]
18. Raja, V.; Murugesan, R.; Solaiappan, S.K.; Arputharaj, B.S.; Rajendran, P.; Al-bonsrulah, H.A.Z.; Thakur, D.; Razak, A.; Buradi, A.; Ketema, A. Design, Computational Aerodynamic, Aerostructural, and Control Stability Investigations of VTOL-Configured Hybrid Blended Wing Body-Based Unmanned Aerial Vehicle for Intruder Inspections. *Int. J. Aerosp. Eng.* **2023**, *2023*, 9699908. [CrossRef]
19. Wang, Y.; Zhu, H.; Zhao, Z.; Zhang, C.; Lan, Y. Modeling, System Measurements and Controller Investigation of a Small Battery-Powered Fixed-Wing UAV. *Machines* **2021**, *9*, 333. [CrossRef]
20. Wang, W.; Zhu, J.; Kuang, M.; Yuan, X.; Tang, Y.; Lai, Y.; Chen, L.; Yang, Y. Design and hovering control of a twin rotor tail-sitter UAV. *Sci. China Inf. Sci.* **2019**, *62*, 194202. [CrossRef]
21. Li, B.; Zhou, W.; Sun, J.; Wen, C.-Y.; Chen, C.-K. Development of Model Predictive Controller for a Tail-Sitter VTOL UAV in Hover Flight. *Sensors* **2018**, *18*, 2859. [CrossRef] [PubMed]
22. Liu, Z.; Guo, J.; Li, M.; Tang, S.; Wang, X. VTOL UAV Transition Maneuver Using Incremental Nonlinear Dynamic Inversion. *Int. J. Aerosp. Eng.* **2018**, *2018*, 6315856. [CrossRef]

23. Ajel, A.R.; Humaidi, A.J.; Ibraheem, I.K.; Azar, A.T. Robust Model Reference Adaptive Control for Tail-Sitter VTOL Aircraft. *Actuators* **2021**, *10*, 162. [CrossRef]

24. Liu, Z.; Gou, L.; Fan, D.; Zhou, Z. Design of Gain-Scheduling Robust Controller for Aircraft Engine. In Proceedings of the 2019 Chinese Control Conference (CCC), Guangzhou, China, 27–30 July 2019; pp. 27–30.

25. Cao, C.; Patel, V.; Reddy, K.; Hovakimyan, N.; Wise, K. Are Phase and Time-Delay Margins Always Adversely Affected by High-Gain? In Proceedings of the Aiaa Guidance, Navigation, & Control Conference & Exhibit, Monterey, CA, USA, 5–8 August 2006.

26. Cao, C.; Hovakimyan, N. Design and Analysis of a Novel L1 Adaptive Controller, Part I: Control Signal and Asymptotic Stability. In Proceedings of the American Control Conference, Minneapolis, MN, USA, 14–16 June 2006.

27. Cao, C.; Hovakimyan, N. Design and Analysis of a Novel L1 Adaptive Controller, Part II: Guaranteed Transient Performance. In Proceedings of the American Control Conference, Minneapolis, MN, USA, 14–16 June 2006.

28. Xargay, E.; Hovakimyan, N.; Cao, C. L1 adaptive controller for multi-input multi-output systems in the presence of nonlinear unmatched uncertainties. In Proceedings of the American Control Conference, Seattle, WA, USA, 11–13 June 2008.

29. Sartori, D.; Quagliotti, F.; Capello, E.; Guglieri, G. Design and Validation of a L1 Adaptive Controller for a mini-UAV Autopilot. 2012, 69, 109–118. *J. Intell. Robot. Syst.* **2012**, *69*, 109–118.

30. Raj, N.; Banavar, R.; Abhishek; Kothari, M. Attitude Control of Novel Tail Sitter: Swiveling Biplane-Quadrotor. *J. Guid. Control. Dyn.* **2020**, *43*, 599–607. [CrossRef]

31. Chipade, V.S.; Abhishek; Kothari, M.; Chaudhari, R.R. Systematic design methodology for development and flight testing of a variable pitch quadrotor biplane VTOL UAV for payload delivery. *Mechatronics* **2018**, *55*, 94–114. [CrossRef]